

Nuclei quadrupole deformation and the weakening of centrally depleted structures using the deformed relativistic Hartree–Bogoliubov theory in continuum

Chan Hoi Yat 3035976765

Introduction

The "bubble" structure in a nucleus is marked by a low-density region at its centre. This feature is commonly associated with the low occupation of s-state orbitals near the Fermi level [1,2] in spherical nuclei. However, this explanation does not hold for deformed nuclei, where the presence of a weakened bubble structure and high central density can be observed even with low probabilities of s-state occupation. In this study, we investigate the relationship between nucleus deformation and its impact on central density.

Method

To quantify the extent of central depletion of nuclei, we introduce the depletion factor (DF), defined for spherical nuclei [1] to be:

$$DF = \left(1 - \frac{\rho_c}{\rho_{\max}}\right) \times 100\% \quad (1)$$

where ρ_c is the nucleon density at the centre, and ρ_{\max} the maximum nucleon density. Although this equation works for spherical nuclei due to the rotational symmetry, we must devise a new formula for the DF for deformed nuclei, where ρ_{\max} is no longer constant [2]. We define $\bar{\rho}_{\max}$ to be the average maximum density for a deformed nuclei. We first find the total charge by summing all $\rho_{\max} dl$ for $0 < \theta \leq 2\pi$, and dividing by the total length.

By the definition of the arclength $l = r\theta$,

$$dl = r_{\max} d\theta \quad (2)$$

where r_{\max} is the radial distance from the centre of the nuclei to ρ_{\max} at a certain θ , so

$$\bar{\rho}_{\max} = \frac{\int_0^{2\pi} \rho(r_{\max}, \theta) r_{\max}(\theta) d\theta}{\int_0^{2\pi} r_{\max}(\theta) d\theta} \quad (3)$$

To check the validity of this equation, we perform dimensional analysis:

$$\frac{\int_0^{2\pi} [\text{Cm}^{-1}][\text{m}]}{\int_0^{2\pi} [\text{m}]} = [\text{Cm}^{-1}] \quad (4)$$

as well as applying the formula for spherical nuclei, where $r_{\max} = R$ and ρ_{\max} are constant with respect to θ and so can be pulled out of the integral:

$$\bar{\rho}_{\max} = \frac{\rho_{\max} R \int_0^{2\pi} d\theta}{R \int_0^{2\pi} d\theta} = \rho_{\max} \quad (5)$$

Therefore, for deformed nuclei, the depletion factor is defined to be:

$$DF = \left(1 - \frac{\rho_c}{\bar{\rho}_{\max}}\right) \times 100\% \quad (6)$$

To calculate DF, values of $\rho(r, \theta)$ are needed, which can be calculated using

$$\rho(r, \theta) = \sum_{\lambda=2n} \rho_{\lambda}(r) P_{\lambda}(\cos(\theta)) \quad (7)$$

for values of $n = 0, 1, 2, 3$. $\rho_\lambda(r)$ is provided by the dRHBC code, and $P_\lambda(\cos(\theta))$ are the Legendre polynomials in $\cos(\theta)$ [3].

To visualise this, heat maps of the nuclei density is plotted, with a blue line tracing the area of maximum $\rho(r, \theta)$. $\bar{\rho}_{max}$ is calculated by taking the total charge traced divided by the total length. Figures 1a), b), c) show the density heat map of Eu 135, 179, and 189 respectively.

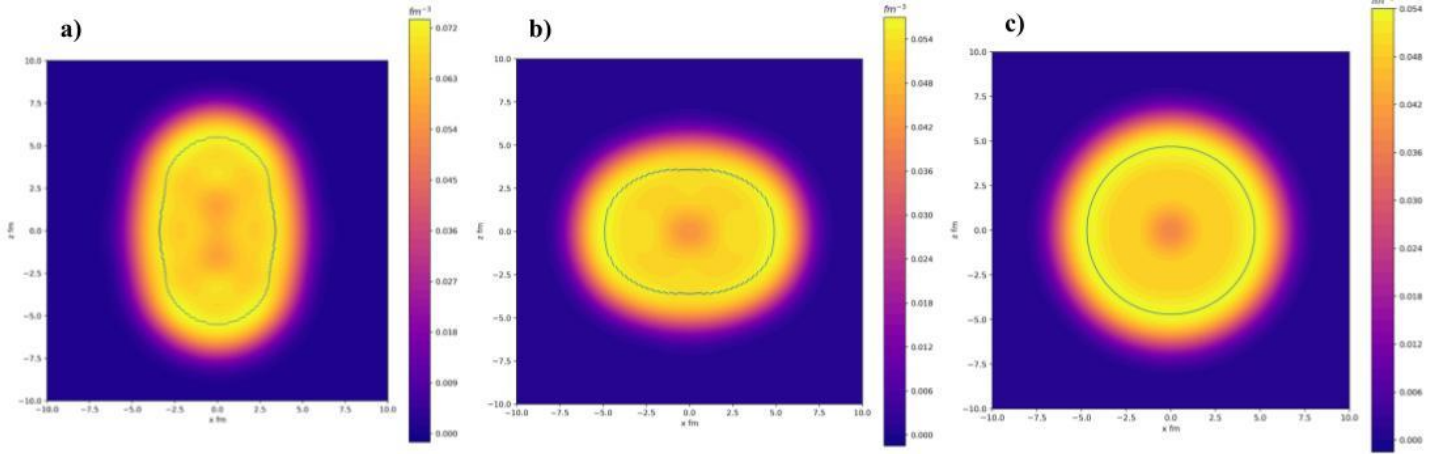


Figure 1: Density heatmaps of nuclei of Eu 135 (a), Eu 179 (b), and Eu 189 (c)

As the calculations of $\bar{\rho}_{max}$ is done using Python, $d\theta$ must be small enough that the results are accurate, and the runtime is short to maximise efficiency. Hence, a twin-axis plot is produced, graphing runtime and values of $\bar{\rho}_{max}$ for varying $d\theta$. Eu 135, 179, and 189 are chosen again to encompass prolate, oblate, and spherical nuclei, and are plotted in Figures 2a), b), c) respectively.

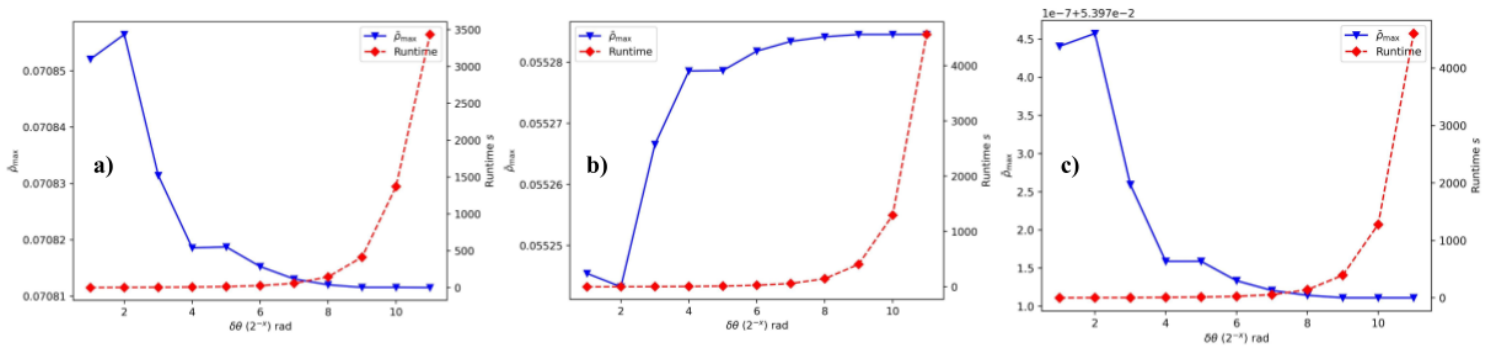


Figure 2: Runtime-convergence graph of nuclei Eu 135 (a), Eu 179 (b), and Eu 189 (c)

We can see that while solutions for $\bar{\rho}_{max}$ converge (blue line) when $d\theta = 2^{-9} \text{ rad}$, the runtime is on average 400 seconds. The percentage difference $\Delta\bar{\rho}_{max}$ between $\bar{\rho}_{max}$ calculated at $d\theta = 2^{-9} \text{ rad}$ and at $d\theta = 2^{-11} \text{ rad}$ is on average $3.5 \times 10^{-5}\%$, which is not necessary for our purposes thus not ideal.

However, for a choice of $d\theta = 2^{-6} \text{ rad}$, the runtime decreases drastically; an average of 30 seconds, yielding $\Delta\bar{\rho}_{max} \approx 0.005\%$. This choice of $d\theta$ has a good balance of runtime and accuracy, and hence is adopted for all further calculations. Now, the deformation parameters (Figure 3) can be plotted along with the DF (Figure 4). In this study, we focus on Eu 189-203.

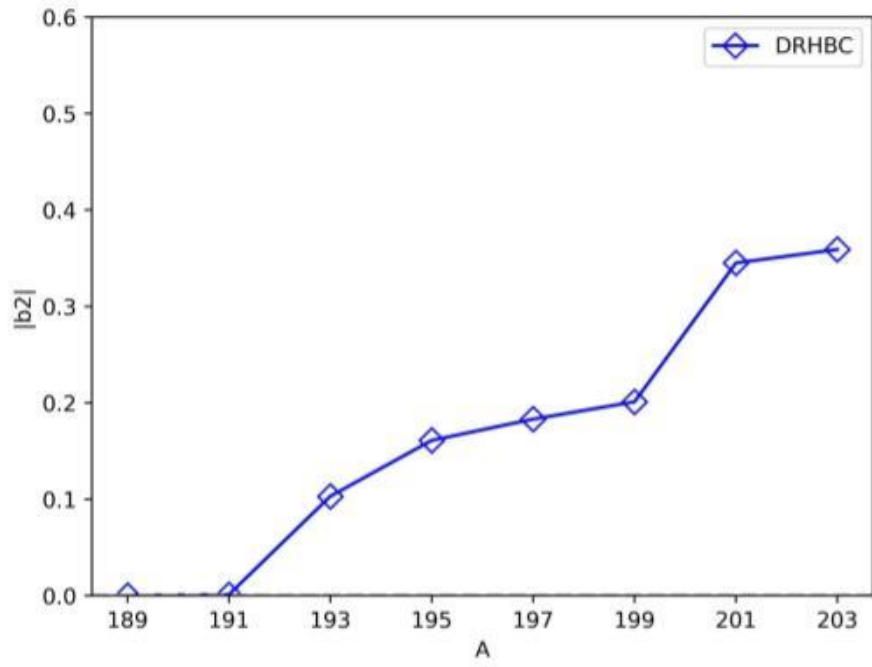


Figure 3: Graph of absolute value of quadrupole deformations for nuclei Eu 189-203

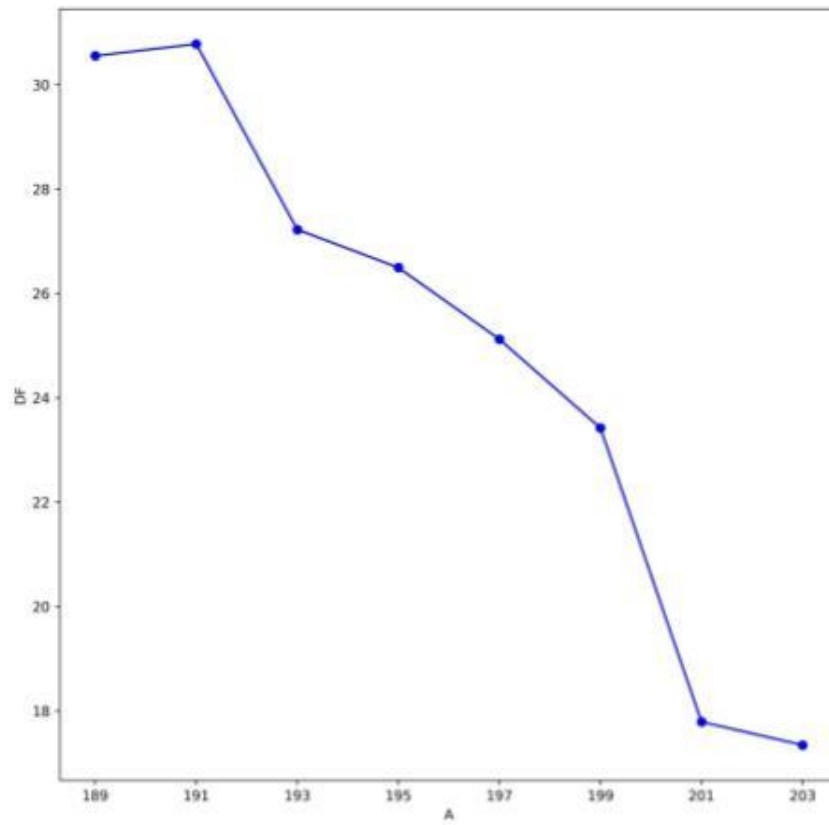


Figure 4: Evolution of depletion factor for nuclei Eu 189-203

Discussion

From Figures 3 and 4, we can see that a general increase in deformation is accompanied by a general decrease in depletion factor, which suggests an increase in the ratio $\rho_c/\bar{\rho}_{max}$ as shown in Equation 6. Hence, we can look at the contributions to central density by different single particle levels in the nucleus and how it changes with deformation [4].

Regarding Eu 189, it's worth noting that the nucleus is spherical due to the magic number of neutrons $N=126$. Previous literature [1, 2] attribute the central depletion in spherical nuclei to the low occupation of the s-orbital near the Fermi surface. Figures 5a) and b) illustrate the density contributions and occupational probabilities of each single particle level.

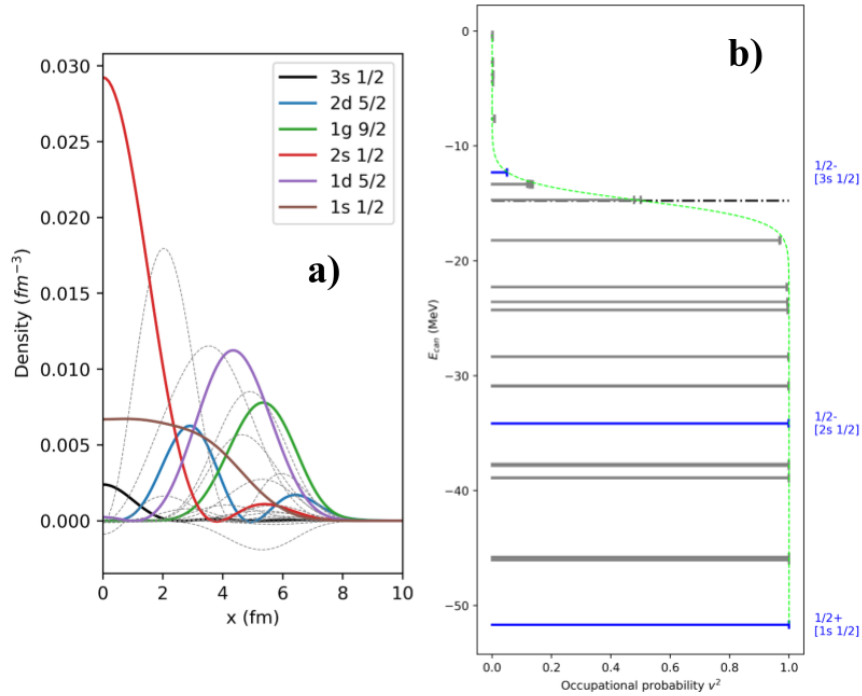


Figure 5: Density contributions of single particle levels and occupational probabilities of s-state orbitals for Eu 189

From the figure, central density is contributed by only the s-state orbitals. However, due to the low occupational probability of the 3s1/2 level, the contribution to central density is minimal, less than that of 1s1/2 and 2s1/2 [5], hence a low value of ρ_c , leading to the high DF seen in Figure 4. However, as we move across to Eu 193, this is where the first large spike in deformation (Figure 3) can be seen.

In Figure 6, the occupational probability of the 3s1/2 orbital decreases, resulting in a reduced contribution to the central density. However, due to orbital splitting caused by a non-zero deformation parameter [4], a non-s state orbital 2d5/2 contributes to the central density instead. Therefore, although the central contribution from the 3s1/2 orbital decreases, it is compensated by the contribution from the 2d5/2 orbital through orbital mixing.

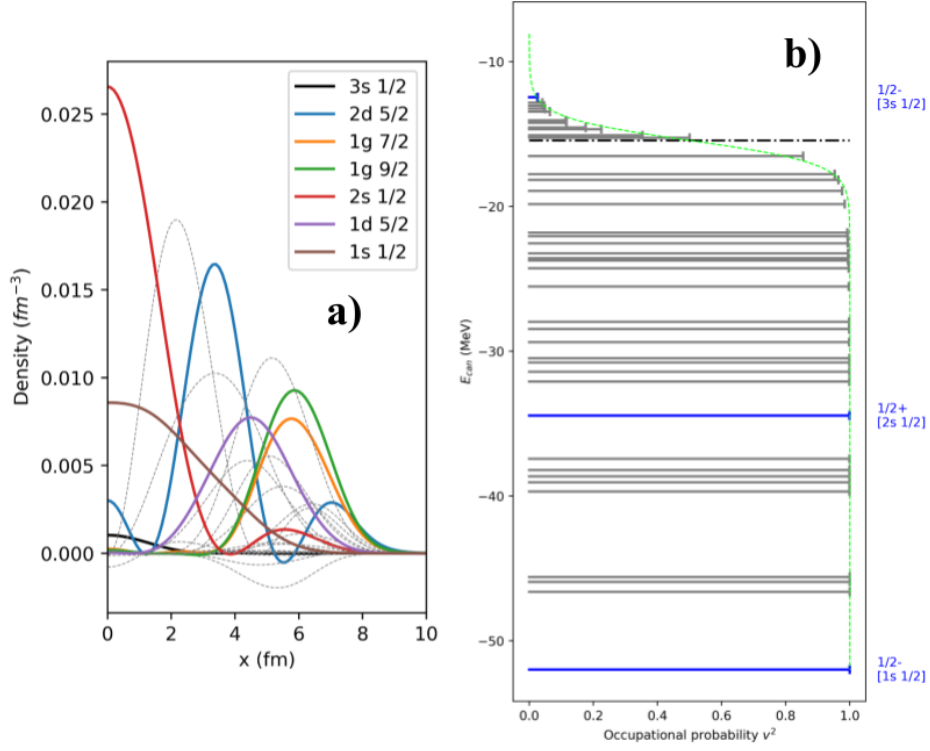


Figure 6: Density contributions of single particle levels and occupational probabilities of s-state orbitals for Eu 193

Furthermore, for increasingly deformed nuclei, orbital mixing becomes more pronounced. For example, in Eu 199 (Figure 7), the contribution of the $3s1/2$ orbital drops to zero, but it reappears as a mixed orbital with $2d5/2$. Due to its higher occupational probability, its contribution approaches that of the $1s1/2$ orbital. Further deformation and orbital mixing lead to increased contributions from non-s orbitals like $1g9/2$, $1d5/2$, etc..

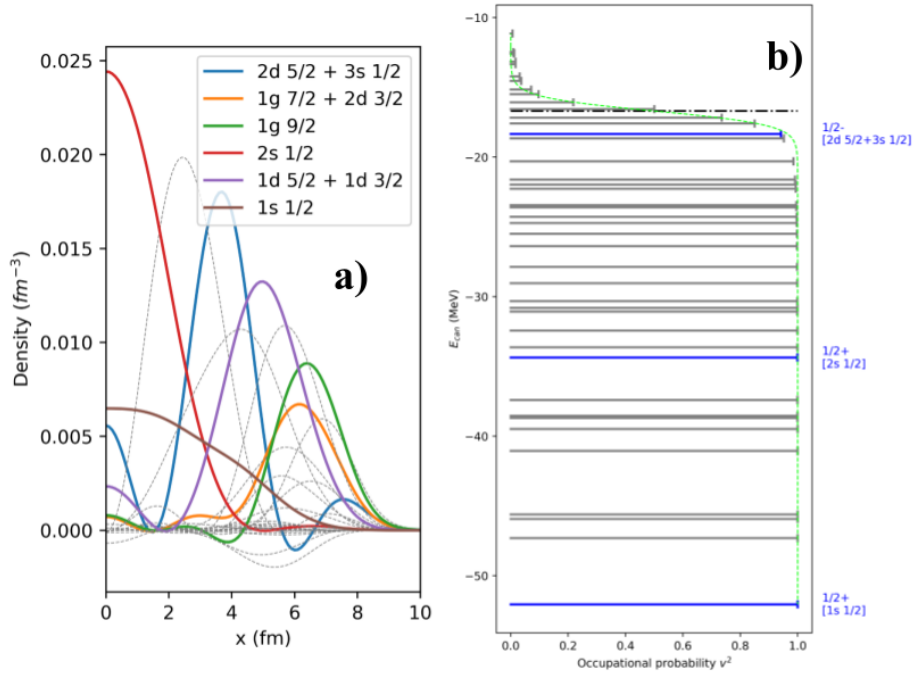


Figure 7: Density contributions of single particle levels and occupational probabilities of s-state orbitals for Eu 199

Following the final spike in deformation from Eu 199 to 201, the densities due to non-s orbitals at $x=0$ increases even more, and more orbital mixing occurs (green; $1g_{9/2} + 2d_{5/2}$). Furthermore, the occupational probability of the $2d_{5/2} + 3s_{1/2}$ single particle level increases to 1.0, causing it to surpass even the contribution of $1s_{1/2}$.

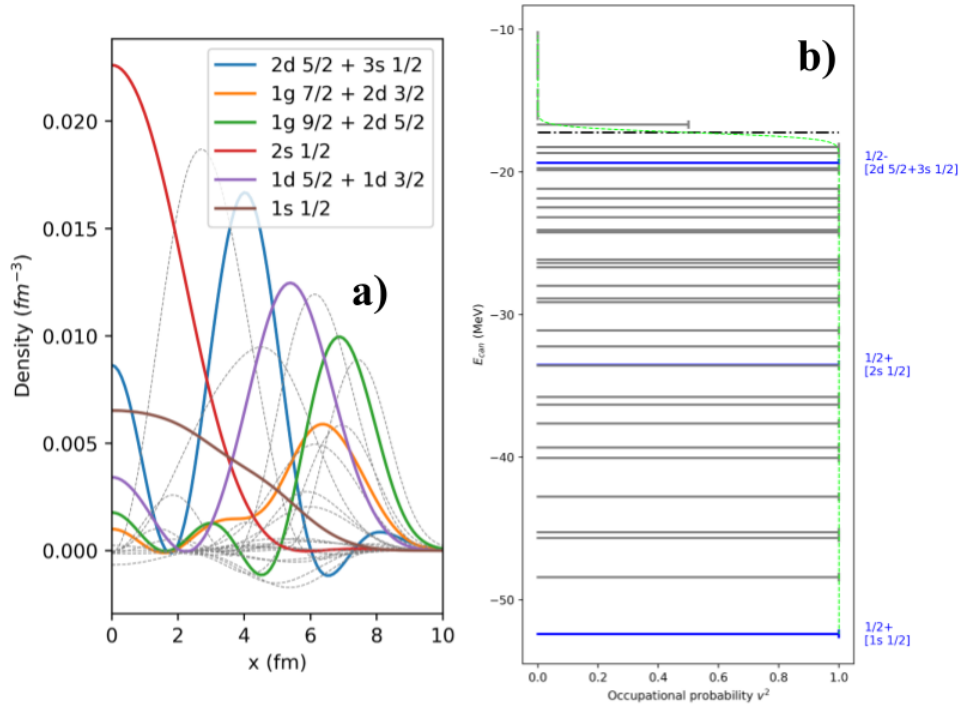


Figure 8: Density contributions of single particle levels and occupational probabilities of s-state orbitals for Eu 201

Conclusion

The presence of non-zero quadrupole deformation results in orbital mixing of single particle levels. This mixing allows non-s state orbitals to contribute to the central density, leading to an increase in central density with deformation and a subsequent decrease in DF. Additionally, the occupational probability of single particle levels also increases, further enhancing their contribution. The shift away from central depletion is evident in Figure 9, where the total density at the nucleus center evolves from a convex to concave profile when focusing on the curves at $x=0$.

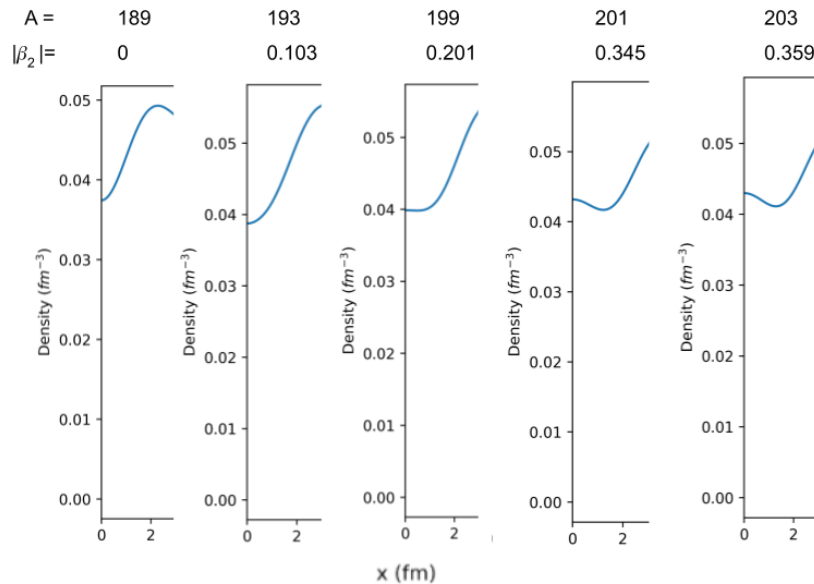


Figure 9: The total density for Eu 189 - 203, showing the transition away from centrally depleted structure for increasing deformation parameter

Bibliography

- [1] Saxena G, M. Kumawat, Kaushik M, Jain SK, Aggarwal M. 2019. Bubble structure in magic nuclei. *Physics Letters B*. 788:1–6. doi:<https://doi.org/10.1016/j.physletb.2018.08.076>.
- [2] Yoon Ha Choi, Lee C-H, Mun M-H, Kim Y. 2022. Bubble nuclei with shape coexistence in even-even isotopes of Hf to Hg. *Physical Review C*. 105(2). doi:<https://doi.org/10.1103/physrevc.105.024306>.
- [3] Zhang K, Cheoun M-K, Choi Y-B, Chong PS, Dong J, Dong Z, Du X, Geng L, Ha E, He X-T, et al. 2022. Nuclear mass table in deformed relativistic Hartree–Bogoliubov theory in continuum, I: Even–even nuclei. *Atomic Data and Nuclear Data Tables*. 144:101488. doi:<https://doi.org/10.1016/j.adt.2022.101488>.
- [4] Luo Z-J, Yu K, Zhou X, Cui J, Sagawa H. 2018 Nov 1. Effects of deformation, pairing and tensor correlation on the evolution of bubble structure within the Skyrme-Hartree-Fock method. *The European Physical Journal A*. doi:<https://doi.org/10.1140/epja/i2018-12620-5>.
- [5] Perera UC, Afanasjev AV. 2022. Bubble nuclei: Single-particle versus Coulomb interaction effects. *Physical Review C*. 106(2). doi:<https://doi.org/10.1103/physrevc.106.024321>.